Classification of Viable and Compromised Flaps with Convolutional Neural Networks: A Preliminary Study

Dite Geovani, Siti Nurmaini, *Member, IAENG,* Anita Desiani, *Member, IAENG,* and Mufida Muzakkie

***Abstract*—A flap is a reconstructive surgical procedure used to repair defects in parts of the human body due to accidents or health complications. Observing flap vitality in the postoperative period is crucial for determining the success rate of flap reconstruction surgery. This observation aims to detect disturbances in the flap as early as possible, allowing medical personnel to intervene immediately. One of the clinical parameters used to assess flap vitality is the flap color. This study classifies viable and compromised flap images using Convolutional Neural Network (CNN) architectures. The stages carried out in this study include pre-processing, classification using CNN architectures, and performance evaluation. The pre-processing steps include resizing, augmentation, and color enhancement. Color enhancement is achieved by increasing the intensity of the saturation component in the HSV color model. The performance evaluation of the color enhancement process yielded an average SSIM of 0.98 and a mean saturation level of 0.9. This indicates that enhanced-color images retain a structure similar to the original image while exhibiting high saturation levels. The CNN architectures used are DenseNet-201, Xception, EfficientNet, and ResNet-50. The performance evaluation results for the classification of viable and compromised flap images demonstrated the following: accuracy, sensitivity, specificity, and F1-score all exceeding 98% G-mean exceeding 97%, and MCC exceeding 93%. This indicates that CNN architectures are capable of classifying viable and compromised flap images precisely and accurately.**

***Index Terms*—Flap, Classification, CNN, Viable, Compromised**

I. Introduction

FLAP is a reconstructive surgical procedure used to repair damage or abnormalities in human body parts due to accidents or health complications such as tumor eradication and infections [1]–[4]. A flap is performed by transferring healthy tissue from a donor site to a defective area at the recipient site. A characteristic feature of a flap is that part of the flap remains attached to the donor area [1]. The part that remains attached to the donor area functions as a blood supply to maintain the vitality of the flap. One of the flap surgery techniques is the free flap surgery technique, also known as free tissue transfer. The free flap technique is a flap surgical technique where the flap is completely removed from the donor area and moved to a recipient area that is located far away. The free flap technique is carried out by connecting the blood vessels in the flap with the blood vessels in the recipient area so that the flap can survive on the blood supply from the recipient area [1].

Observation of flap vitality in the postoperative period is an important aspect in determining the success rate of flap reconstruction surgery. Observation aims to detect disturbances in the flap as early as possible so that medical personnel can intervene immediately. Early interventions to maintain flap success can have a higher success rate [5]. One of the clinical parameters used to assess flap vitality is flap color [6]. A flap that matches the color of the patient's skin or body as a whole is considered to have good vitality and is called a viable flap. A bluish or purplish flap indicates venous congestion and is called a compromised flap.

Observation of flap vitality needs to be performed strictly by medical personnel every 12 to 24 hours. The results of the free flap technique require stricter observation, with monitoring every hour for the first 48 hours [7]. Physical examination is a method of observing flap vitality that is performed repeatedly. The flap vitality observation method has several disadvantages, including subjectivity, time consumption, environmental influences around the flap, the competency level of medical personnel, and the need for trained human resources [7]. There is a need to develop technology for observing flap vitality to assist medical personnel in conducting vitality observations and determining early interventions.

One use of technology to observe flap vitality is the automatic classification of flap images. Classification involves grouping objects or assigning them specific labels or categories [8]–[10]. Automatic image classification has been developed using deep learning algorithms. Deep learning is a subset of machine learning that is popular in the medical field. Deep learning, uses deep neural networks to automatically learn hierarchical features from data [11]. Deep learning has strong capabilities in integrating large image datasets, learning complex relationships in images,

Manuscript received September 12, 2024; revised April 2, 2025.

This research was funded by the Ministry of Education, Culture, Research, and Technology of the Republic of Indonesia through the PMDSU scheme research funding program under contract 0017.002/UN9/SB1.LP2M.PT/2024 and supported by the Intelligent System Research Group Laboratory.

Dite Geovani is a PhD candidate of the Engineering Faculty, Universitas Sriwijaya, Palembang 30139, Indonesia. (e-mail: ditegeovani@gmail.com).

Siti Nurmaini is a Professor of Computer Engineering, Intelligent, System Research Group, Universitas Sriwijaya, Palembang 30139, Indonesia. (corresponding author to provide phone: +62-852-6804-8092; e-mail: sitinurmaini@gmail.com).

Anita Desiani is an Assistant Professor of Mathematics Department, Universitas Sriwijaya, Indralaya 30662, Indonesia. (e-mail: anita_desiani@unsri.ac.id).

Mufida Muzakkie is a PhD candidate of the Medicine Faculty, Universitas Sriwijaya, Palembang 30139, Indonesia. (e-mail: mufida.muzakkie@gmail.com).

and combining existing knowledge or patterns [10], [12]. One of the deep learning algorithms widely used for image processing in the medical field is the Convolutional Neural Network (CNN) [13]. CNN is an artificial neural network that can accept raw input data, such as images [14]. CNN can be used in several pattern recognition tasks, such as image classification [15], [16]. The main structure of CNN consists of several layers such as convolutional layers, pooling layers, and fully connected layers [17]–[19]. CNN is able to work automatically in recognizing complex patterns in images [20]–[23]. Several studies have applied CNN architectures to image classification in the medical field. Halit & Ibrahim [24] applied the DenseNet201 architecture to classify cataracts on retinal fundus images, Moataz et al. [25] applied the Xception architecture to classify skin cancer on skin images, Zulfiqar et al. [26] applied the EfficientNet architecture to classify brain tumors on brain MRI images, and Kesuma & Rudiansyah [27] applied the ResNet-50 architecture to classify COVID-19 on lung images.

Research on CNNs for the classification of viable and compromised flaps is yet to be extensively explored. This is due to the limited availability of flap image data. Flap image data is private and cannot be easily accessed by anyone except authorized parties at the hospital. In this study, the classification of viable and compromised flaps will be performed on flap images using CNN architectures. The flap image data used in this study is private and has been approved by the hospital for use. The flap image data used is the result of camera capture, so pre-processing stages are needed to increase the amount of image data and improve image quality. The success rate of viable and compromised flap classification using the proposed CNN architecture will be evaluated by measuring classification performance evaluation.

II. MATERIAL AND METHODS

A. Data Description

This study used flap image data provided by the hospial. This data is private data that cannot be accessed publicly. The flap image data amounted to 935 images consisting of 425 viable flaps and 510 compromised flaps. Flap image data has different image sizes in .jpg, .png, and .jpeg formats. A sample of flap image data used in this study is shown in Fig. 1.

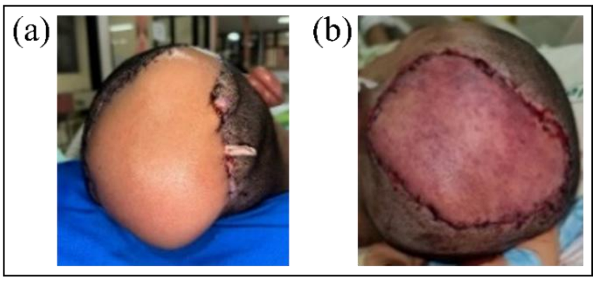

Fig. 1. A Sample of (a) A Viable and (b) A Compromised Flap Data

B. Pre-processing

In the pre-processing stage, several steps will be taken to increase the amount of image data and enhance image quality. Several pre-processing stages that will be carried out in this study include resizing, augmentation, and color enhancement.

Resizing

Resizing is the process of adjusting the image size so that it is uniform [27]–[31]. Resizing is done to ensure the image size is uniform and adapted to the architecture to be used [10]. In this study, all flap images will be resized to 224×224 pixels.

Augmentation

Image augmentation is a process of creating new images from the original image and increasing data variance to enhance the amount of image data [32]–[35]. In deep learning, augmentation can improve model generalization, train models to be more robust, and increase model accuracy [33], [36]–[38]. The image augmentation method that will be used in this study is flipping. The flipping method will be applied horizontally, vertically, and both horizontally and vertically to produce three new images from each original image. Fig. 2 illustrates the flip augmentation method used in this study.

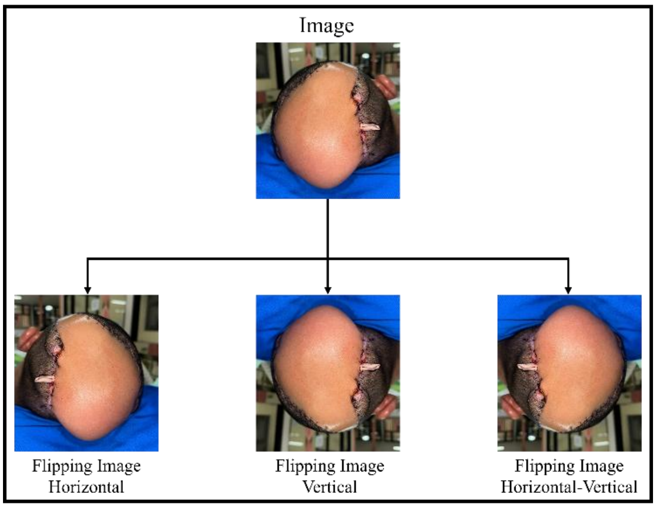

Fig. 2. An Example of The Application of The Flip Augmentation Method

Color Enhancement

In the color enhancement stage, color enhancement is applied to the flap images to improve their clarity. Color enhancement aims to enhance the colors and characteristics of the images [39], [40]. Color enhancement is implemented by increasing the intensity of the saturation characteristic of the HSV color model [41]. In this study, color enhancement was performed by intensifying the saturation in the red channel of the HSV color model. This adjustment was applied to compromised flap images to highlight the differences in appearance between viable and compromised flap images. An example of a color-enhanced flap image can be seen in Fig. 3.

Fig. 3. An Example of A Color-enhanced Flap Image

C. Convolutional Neural Networks (CNN) Architectures

DenseNet-201 Architecture

DenseNet is an architecture consisting of layers connected to every other layer [42], [43]. The DenseNet architecture offers several advantages, including overcoming the vanishing gradient problem, enhancing feature propagation, and reducing the number of parameters [25], [42]. In the DenseNet-201 architecture, the feature map from the preceding layer layer is used as input for each subsequent layer [42]. The DenseNet-201 architecture has deep and complex layers, comprising 201 layers. An illustration of the DenseNet-201 architecture can be seen in Fig.4.

In Fig. 4, it can be seen that the DenseNet-201 architecture has a direct connection pattern from each layer to every other layer. Every n-th layer in the DenseNet-201 architecture receives a feature map from all preceding layers. Based on Figure 3, the DenseNet-201 architecture consists of dense blocks containing interconnected layers, where each layer receives input from all previous layers. Each dense block layer consists of a convolution, batch normalization, ReLU activation function, and transition layers. The output results from the previous layer can be calculated using equation (1).

$$d_n = H_n([d_0, \dots, d_{n-1}]) \tag{1}$$

where, d_n is the feature map or output at the n-th layer and H_n is a representation of the convolution operation, batch normalization, and ReLU activation function [25]. The convolution process applies a convolutional kernel to capture localized patterns from the input. The convolution operation is carried out using equation (2).

$$v_{x,y} = \left(\sum_{o=0}^{n-1}\sum_{p=0}^{n-1} e_{o+x,p+y} \times k_{o+1,p+1}\right) + b_i \tag{2}$$

for $x = 1,2,\dots,n$ and $y = 1,2,\dots,n$, where $v_{x,y}$ represents an element of the convolution matrix in the x-th row of the y-th column, $e_{o+x,p+y}$ is the input matrix entry of the $o+x$-th row of the $p+y$-th column, $k_{o+1,p+1}$ is the $o+1$-th row $p+1$-th column kernel matrix entry, and b_i is bias for the i-th kernel [10].

Batch normalization is a normalization technique applied to each layer in the network [44], [45]. The batch normalization operation performs normalization on the mean (μ_y) and variance (σ_y^2) values. The batch normalization calculation process is defined in equations (3), (4), and (5).

$$\mu_y = \frac{1}{m}\sum_{x=1}^{m} v_{x,y} \tag{3}$$

$$\sigma_y^2 = \frac{1}{m}\sum_{x=1}^{m}\left(v_{x,y} - \mu_y\right)^2 \tag{4}$$

$$g = \hat{v}_{x,y} = \frac{v_{x,y} - \mu_y}{\sqrt{\sigma_y^2 + \varepsilon}} \tag{5}$$

where, μ_y and σ_y^2 are the mean and variance of each mini-batch, j is the number of mini-batches, m is the amount of data in a mini-batch $\hat{v}_{x,y}$ is the normalized matrix entry in the x-th row and j-th column, $v_{x,y}$ is the input matrix entry (convolution result matrix) at the same position, and ε is the smallest constant value [10]. The Rectified Linear Unit (ReLU) is a commonly used activation function in CNNs. In the ReLU activation function, all the inputs to the function are negative, so the output is zero [46], [47]. Mathematically, the ReLU function equation can be seen in the equation (6) [48].

$$r = r(\hat{v}_{x,y}) = \max(0, \hat{v}_{x,y}) = \begin{cases} \hat{v}_{x,y} & jika\ \hat{v}_{x,y} \geq 0 \\ 0 & jika\ \hat{v}_{x,y} < 0 \end{cases} \tag{6}$$

where, r is the ReLU output result and $\hat{v}_{x,y}$ is the input pixel from the batch normalization results [10]. In the DenseNet architecture, there is a sigmoid layer before the output. The sigmoid activation function is used for two-label classification because it has a range of 0 to 1 [49]. The activation function is calculated using equation (7).

$$s = \frac{1}{1+e^{-r}} \tag{7}$$

where, s is the output of the sigmoid activation function and r is the output of the ReLU activation function.

Xception Architecture

Xception is one of the CNN architectures that can improve the efficiency of the computational process. Xception uses depthwise separable convolutions and residual connections, so it has small parameters and an efficient computational process [10]. A key feature of Xception is the use of depthwise separable convolutions rather than convolutional operations [50], [51]. The use of depth-based separable convolutions can reduce the number of parameters so that the architecture is efficient in extracting features and computing processes [52]. Xception comprises both convolutional and separable convolutional layers. In this architecture, depthwise convolution processes information across channels, while pointwise convolution handles information within each channel. This separation enables the network to effectively learn features both between and within different channels [50]. An illustration of the Xception architecture can be seen in Fig. 5.

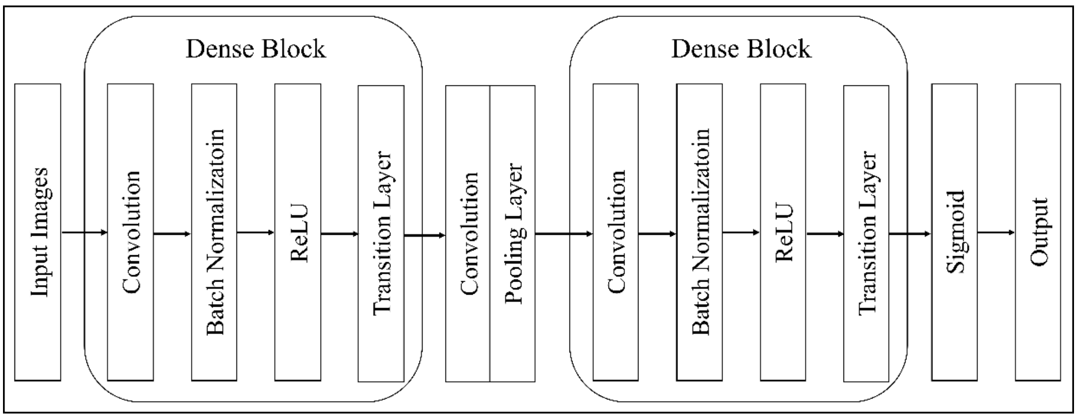

Fig. 4. Illustration of The DenseNet-201 Architecture

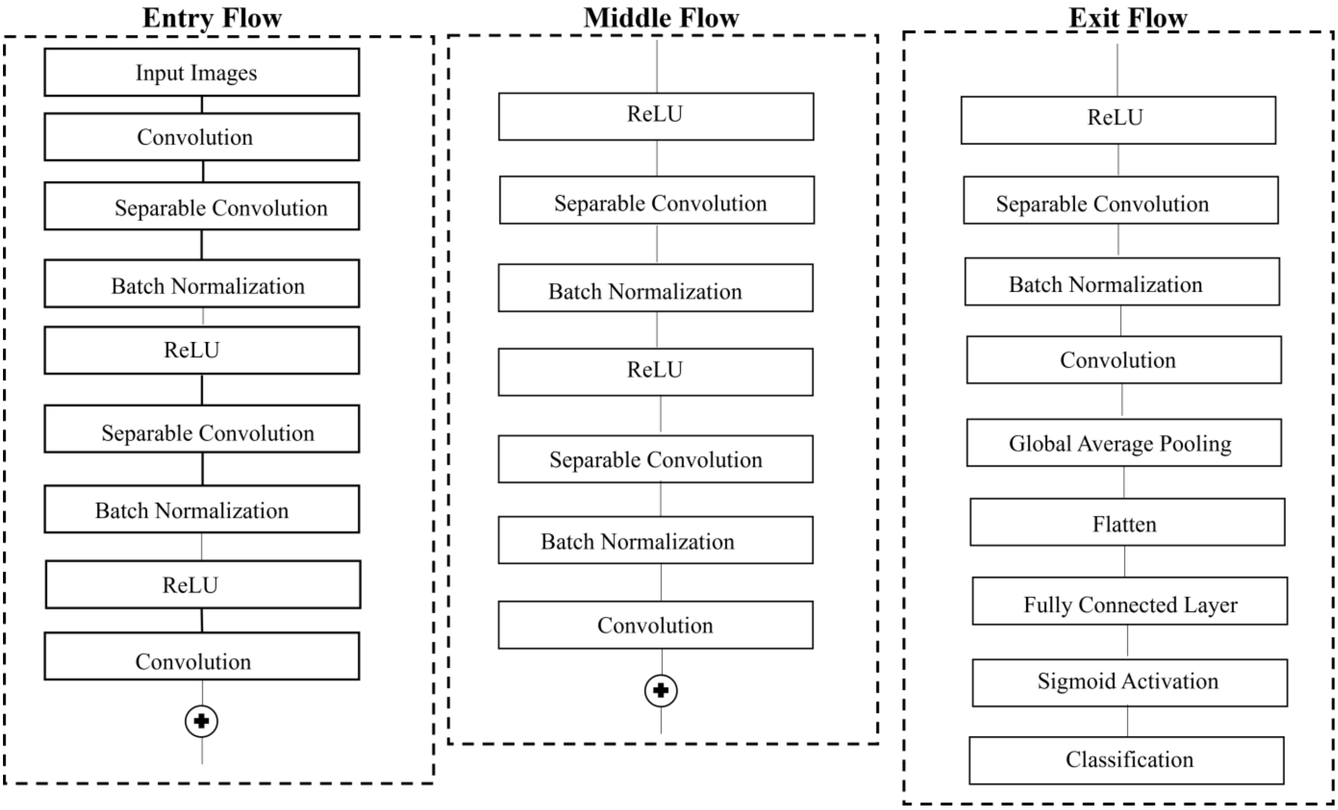

Fig. 5. Illustration of The Xception Architecture

Figure 5 shows that the Xception architecture consists of three parts: input, middle, and output streams. Each part of the Xception architecture uses depthwise separable convolution. The Xception architecture comprises multiple convolutional layers, batch normalization, and ReLU activation functions. In the Xception architecture, the image input is first processed in the input stream block, then continues to the middle stream block, and finally enters the output stream block. A sigmoid function is at the end of the output flow block for class classification. The sigmoid activation function is used because classification is only into two labels: compromised and viable flaps. The convolution operation process, batch normalization, ReLU, and sigmoid activation function are performed using equations (2)-(7).

EfficientNet Architecture

EfficientNet architecture is one of the most efficient CNN architectures for image classification [53]. EfficientNet uses a uniform compound scaling approach to structurally improve CNN architectures by using a fixed set of scaling coefficients. EfficientNet takes an input image with pixel intensity values in the range [0-255] because it performs image normalization automatically. The EfficientNet architecture consists of a stem layer followed by seven blocks and a final layer. An illustration of the layer arrangement of the EfficientNet architecture can be seen in Fig. 6. In Fig. 6, it can be seen that the EfficientNet architecture consists of a stem layer, 7 blocks, and a final layer. The stem layer extracts initial features, which are then further processed by subsequent layers. The stem layer consists of input, rescaling, normalization, zero padding, convolution operations, batch normalization, and activation functions. Modules 1 to 3 in each block consist of depthwise convolution operations, batch normalization, rescaling, convolution operations, and activation functions. The depth level of each block depends on the EfficientNet variant used. The final layer of the EfficientNet architecture consists of convolution operations, batch normalization, and activation functions.

ResNet-50 Architecture

The ResNet-50 architecture is able to handle the gradient vanishing problem because it has residual connections in the layers, thus accelerating the convergence of the deep network [54]. The ResNet-50 architecture has low computational complexity despite its depth [55]. The ResNet-50 architecture can be classified accurately because it extracts more representative features [26], [56]. The ResNet-50 architecture consists of 50 layers. An illustration of the ResNet-50 architecture can be seen in Fig. 7.

In Fig. 7, it can be seen that the ResNet-50 architecture consists of convolution operations, batch normalization, ReLU activation function, max pooling, identity block, average pooling, fully connected layers, and sigmoid activation function. The first operation is a convolution on the input image, followed by batch normalization. The output of the batch normalisation operation is used as input to the ReLU activation function. Max pooling is used to reduce the dimensions of the feature map generated in the previous process. The results of max pooling are used as input for the next convolution. The results of the second convolution are then used as input for the identity blocks. The identity blocks consist of convolution layers, batch normalization, and ReLU activations without feature map merging. The results of the identity blocks become input for the next convolution. In the second to fourth identity blocks, the same process is carried out as in the first identity block. The feature map obtained from the feature learning process used as input for the classification stage. This stage consists of combining global average pooling, fully connected layers, and sigmoid activation functions.

D. Performance Evaluation

Performance evaluation of the color enhancement method used is measured by calculating the structural similarity index measure (SSIM) and mean saturation level. SSIM is used to assess the structural resemblance between color-enhanced images and the original images [57]. The mean saturation level is used to measure the level of richness or intensity of color by measuring the average saturation value of all image pixels.

The evaluation of the classification results performance is represented in the form of a matrix called the confusion matrix, which is generated at the testing stage. In a confusion matrix, the columns represent the actual classes, while the rows represent the predicted classes [58]. The confusion matrix includes terms such as true positive (TP), true negative (TN), false positive (FP), and false negative (FN). This study measures architectural performance based on the confusion matrix by calculating accuracy, sensitivity, specificity, F1-score, geometric mean (G-mean), and Matthews correlation coefficient (MCC). The performance evaluations are calculated using equations (8), (9), (10), (11), (12), and (13) [59]–[63].

$$Accuracy = \frac{TP+TN}{TP+FN+FP+TN} \quad (8)$$

$$Sensitivity = \frac{TP}{TP+FN} \quad (9)$$

$$Specificity = \frac{TN}{TN+FP} \quad (10)$$

$$F1-Score = \frac{2 \times TP}{2 \times TP+FP+FN} \quad (11)$$

$$G-mean = \sqrt{Sensitivity \times Specificity} \quad (12)$$

$$MCC = \frac{TP.TN-FP.FN}{\sqrt{(TP+FP)(TP+FN)(TN+FP)(TN+FN)}} \quad (13)$$

where, TP is the ratio of positive labels classified as positive, TN is the ratio of negative labels classified as negative, FP is the ratio of negative labels classified as positive, and FN is the ratio of positive labels classified as negative [64]. The overall method of this study can be seen in Fig. 8.

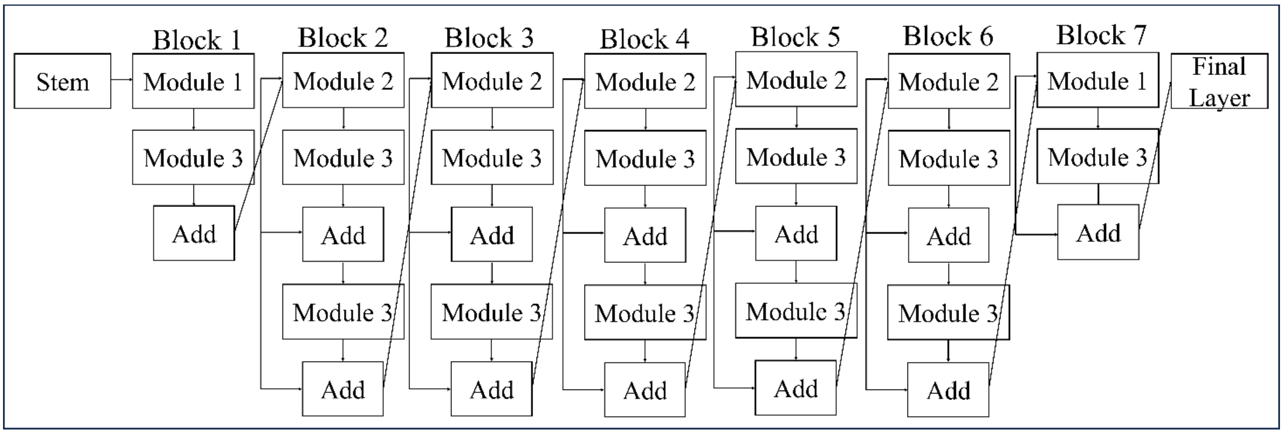

Fig. 6. Illustration of The EfficientNet Architecture

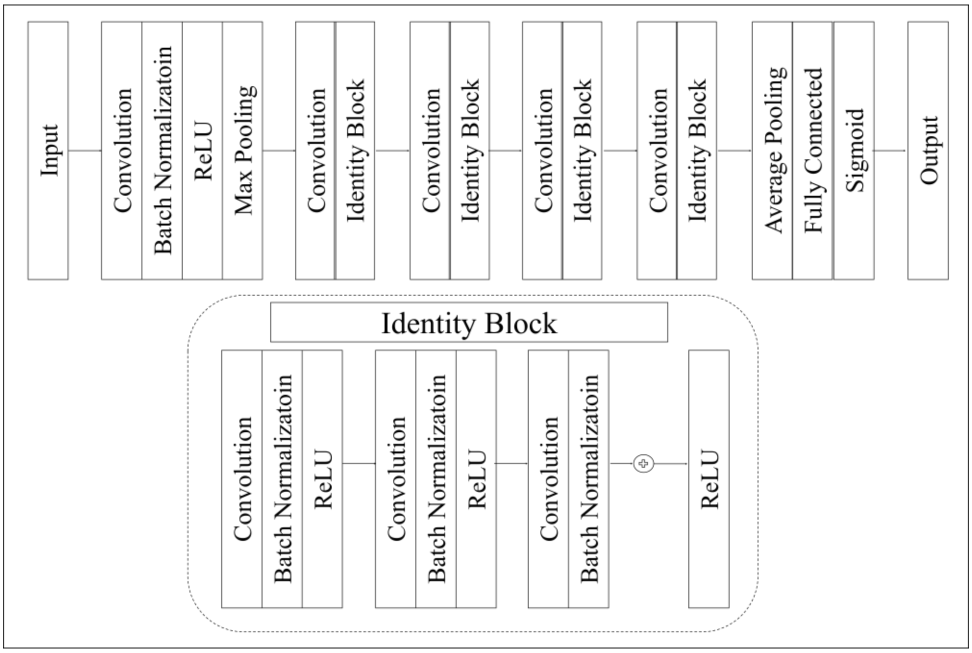

Fig. 7. Illustration of The ResNet-50 Architecture

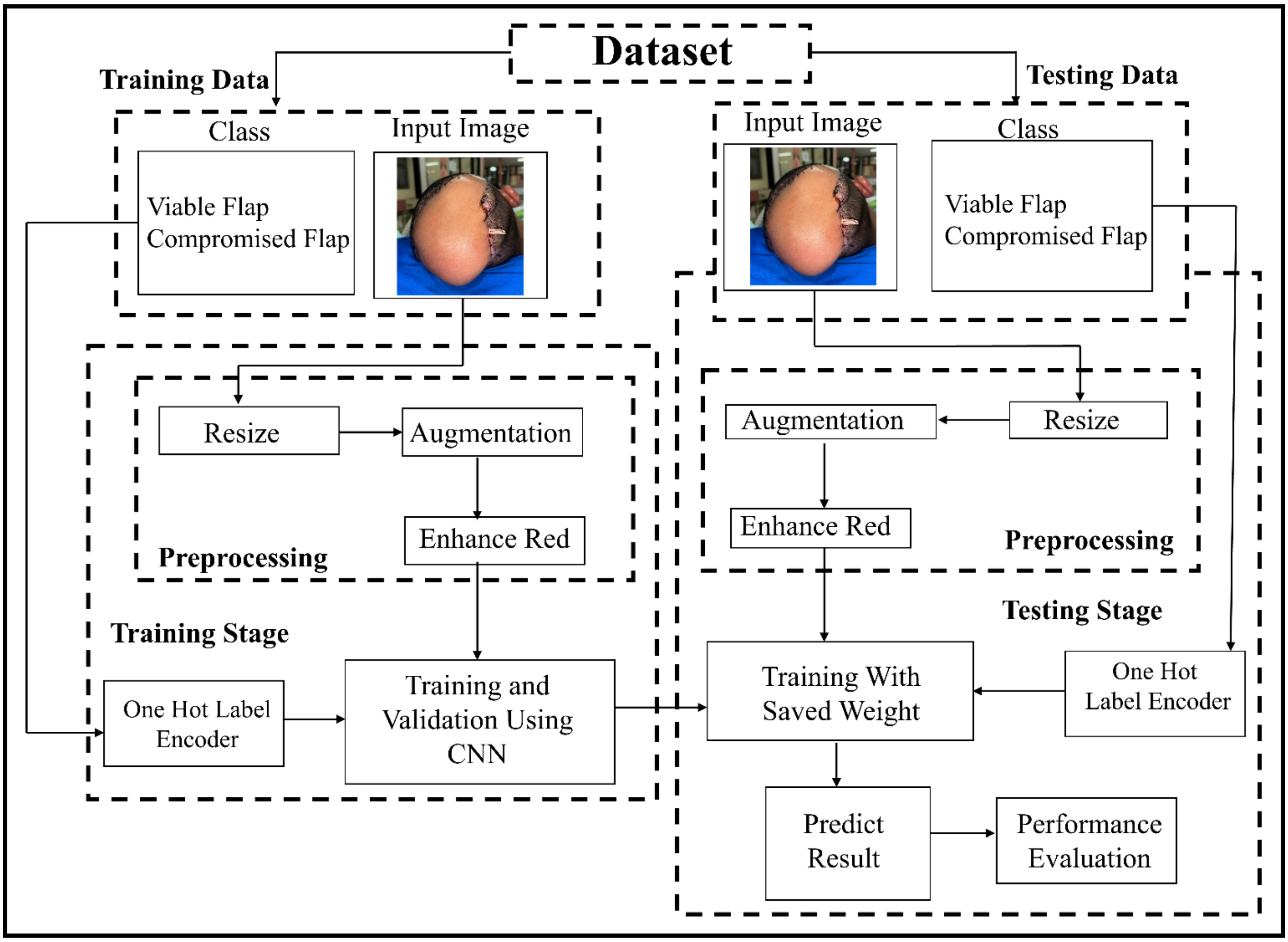

Fig. 8. Proposed Method for Classification of Viable and Compromised Flap

III. Results and Discussion

A. Pre-processing

In the pre-processing stage, resizing, augmentation, and color enhancement are carried out. Resizing is done to make the image size uniform and regular. In the resizing stage, the image size is changed to 224×224 pixels. Augmentation is performed to expand the quantity of image data by varying the original image. The augmentation methods used in this study are vertical, horizontal, and vertical-horizontal flips. The number of images after augmentation became 3,740 images consisting of 1,700 viable flap images and 2,040 compromised flap images.

Color enhancement is carried out to clarify the characteristics and enhance the red color of the compromised flap image. In color-enhanced images, the SSIM and mean saturation level were measured. SSIM is used to assess the structural resemblance between color-enhanced images and the original images The mean saturation level is used to measure the level of richness or intensity of color by measuring the average saturation value of all image pixels. The results of SSIM and mean saturation level measurements on color-enhanced images can be seen in Table 1.

Based on Table 1, the average SSIM value obtained is 0.98. This indicates that the enhanced-color image closely resembles the original structure, as perceived by human vision. The mean saturation level obtained is 0.9. This indicates that enhanced-color images exhibit a high level of color saturation, resulting in a more vivid and striking appearance.

TABLE I
SSIM and Mean Saturation Level on Color-enhanced Images

No	Image	SSIM	Mean Saturation Level
1	Image_1	0.976538	0.896538
2	Image_2	0.977084	0.897084
3	Image_3	0.980938	0.900938
4	Image_4	0.980656	0.900656
5	Image_5	0.979684	0.899684
.	.	.	.
931	Image_931	0.974872	0.894872
932	Image_932	0.974872	0.894872
933	Image_933	0.976643	0.896643
934	Image_934	0.976643	0.896643
935	Image_935	0.976643	0.896643
	Mean	0.980353	0.900353

B. Classification using CNN Architecture

Original Images

This section performs classification using the resized images from the pre-processing stage. Classification consists of two processes: training and testing. The original dataset includes 935 images of 425 viable flaps and 510 compromised flaps. Before the training process, the data is divided into 75% training data, comprising 701 images, and 25% testing data, comprising 234 images. The training data was further separated into 80% training data, comprising 560 images, and 20% validation data, comprising 141 images. Classification is carried out into two labels: viable and compromised flaps. Classification is performed using several CNN architectures: DenseNet-201, Xception, EfficientNet, and ResNet-50. The parameters used in the training process with original images are 100 epochs, a batch size of 5, and the Adam optimizer. During training, the accuracy of both the training and validation data is measured to evaluate the performance of the proposed classification models. Additionally, the loss value is assessed to quantify the error rate between predicted and actual labels. Accuracy and loss graphs from the original image classification training process using DenseNet-201, Xception, EfficientNet, and ResNet-50 architectures are presented in Figs. 9–12.

Based on Figs. 9–12, the original image classification training process using the DenseNet-201, Xception, EfficientNet, and ResNet-50 architectures shows fluctuating accuracy in both the training and validation datasets. In Fig. 9(b) and 12(b), the accuracy values for the DenseNet-201 and ResNet-50 architectures stabilize at 40th epoch towards values above 95%. In Fig. 10(b) and 11(b), the accuracy values for the Xception and EfficientNet architectures stabilize at the 40th and 65th epoch towards values above 95%. Based on Fig. 9(a) and 11(a), the original image classification training process using the DenseNet-20 and EfficientNet architectures has a loss value that continues to decrease close to 0. In Fig. 10(a) and 12(a), the loss value in the Xception and ResNet50 architectures shows a loss value that fluctuates and stabilizes at the 45th epoch approaching 0. The accuracy and loss values obtained during the training process show that these CNN architectures are capable of performing classification accurately and have a low error rate.

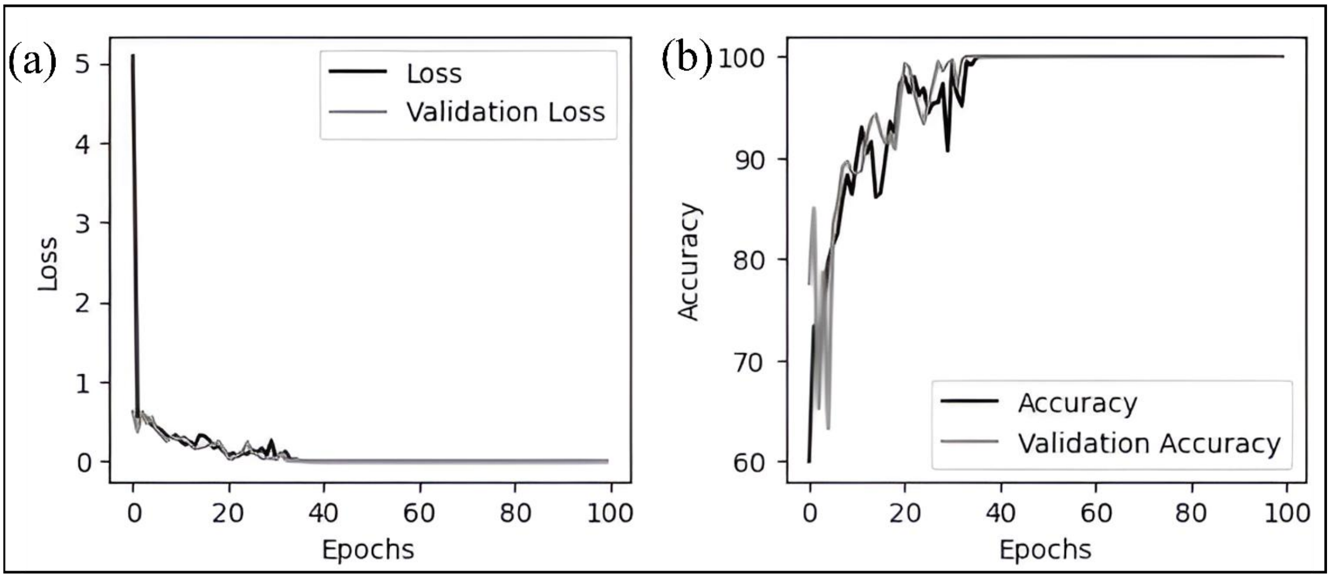

Fig. 9. Graphs of (a) Loss and (b)Accuracy of Original Images Classification during Training with The DenseNet-201 Architecture

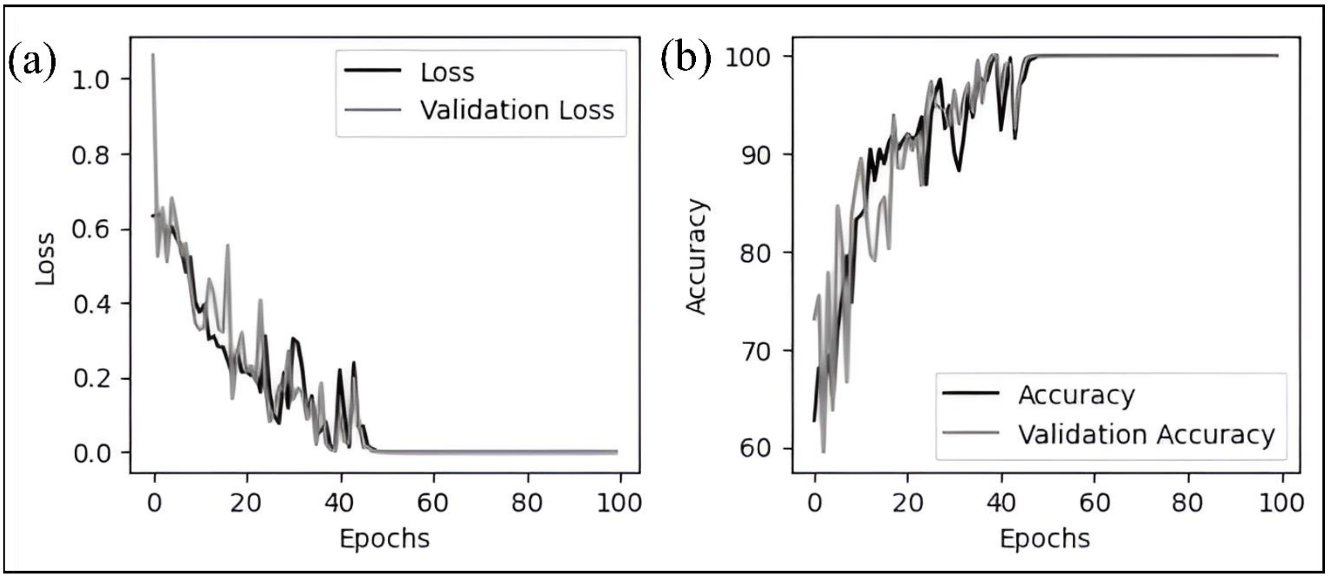

Fig. 10. Graphs of (a) Loss and (b)Accuracy of Original Images Classification during Training with The Xception Architecture

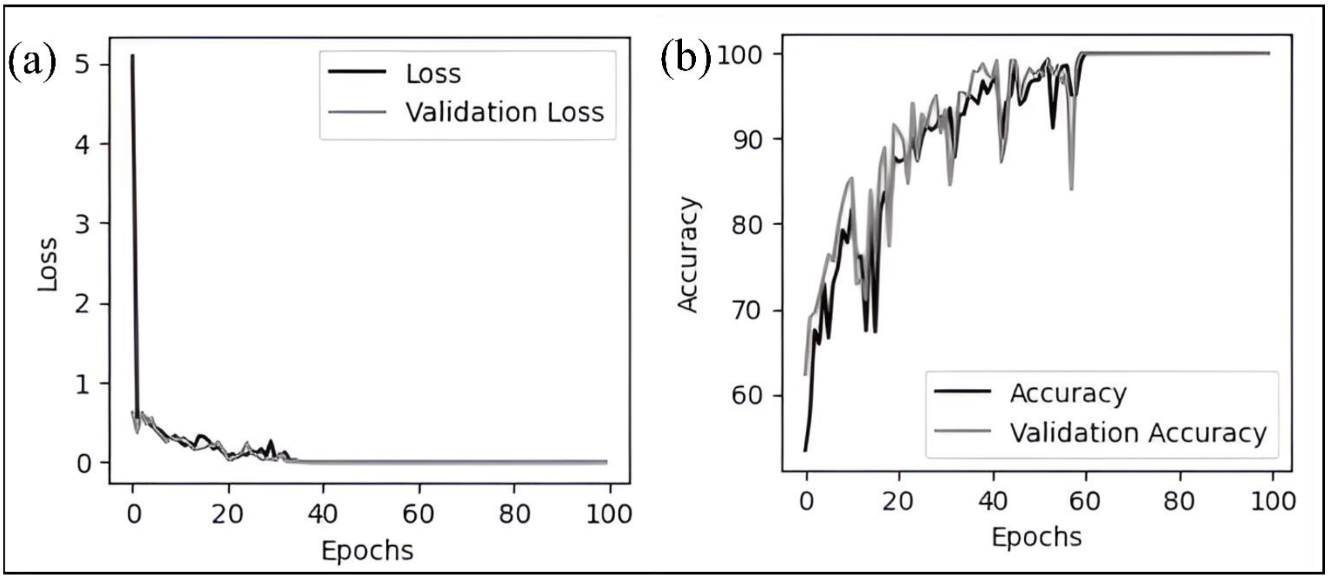

Fig. 11. Graphs of (a) Loss and (b)Accuracy of Original Images Classification during Training with The EfficientNet Architecture

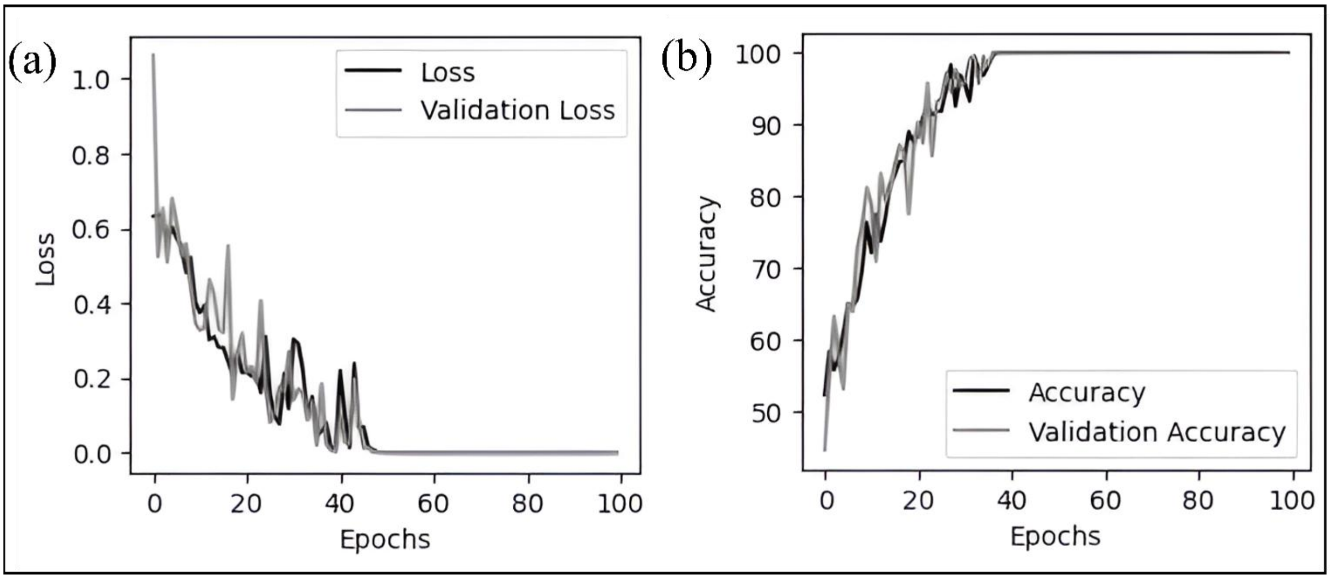

Fig. 12. Graphs of (a) Loss and (b)Accuracy of Original Images Classification during Training with The ResNet-50 Architecture

Augmented Images

In this section, classification is performed using resized and augmented images from the pre-processing stage. Classification includes training and testing. The augmented images include 3,740 images of 1,700 viable flap images and 2,040 compromised flap images. Before the training process, the data was divided into 75% training data, comprising 2,805 images, and 25% testing data, comprising 935 images. The training data was further separated into 80% training data, comprising 2,244 images, and 20% validation data, comprising 561 images. Classification is carried out into two labels, viable and compromised flaps. Classification is performed using several CNN architectures: DenseNet-201, Xception, EfficientNet, and ResNet-50.

The parameters used in the training process with augmented images are 100 epochs, a batch size of 5, and the Adam optimizer. During training, the accuracy of both the training and validation data is measured to evaluate the performance of the proposed classification models. Additionally, the loss value is assessed to quantify the error rate between predicted and actual labels. Accuracy and loss graphs from the original image classification training process using DenseNet-201, Xception, EfficientNet, and ResNet-50 architectures are presented in Figs. 13, 14, 15, and 16.

Based on Figs. 13–16, the augmented image classification training process using the DenseNet-201, Xception, EfficientNet, and ResNet-50 architectures shows fluctuating accuracy in both the training and validation datasets. In Fig. 13(b) and 14(b), the accuracy values of the DenseNet-201 and Xception architectures stabilize at the 45th epoch towards a value above 95%. In Fig. 15(b) and 16(b), the accuracy values on the EfficientNet and ResNet-20 architectures stabilize at the 65th and 30th epochs toward values above 95%. Based on Fig. 13(a), 14(a), 15(a), and 16(a), the training process of augmented image classification using the DenseNet-20, Xception, EfficientNet, and ResNet-50 architectures shows a loss value that fluctuates and is close to 0. The accuracy and loss values obtained during the training process show that these CNN architectures are capable of performing classification and have a low error rate.

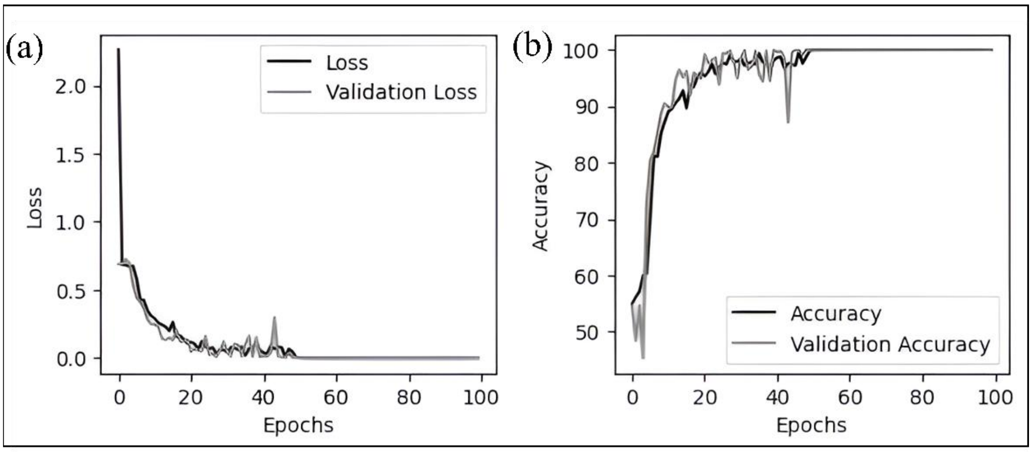

Fig. 13. Graphs of (a) Loss and (b)Accuracy of Augmented Images Classification during Training with The DenseNet-201 Architecture

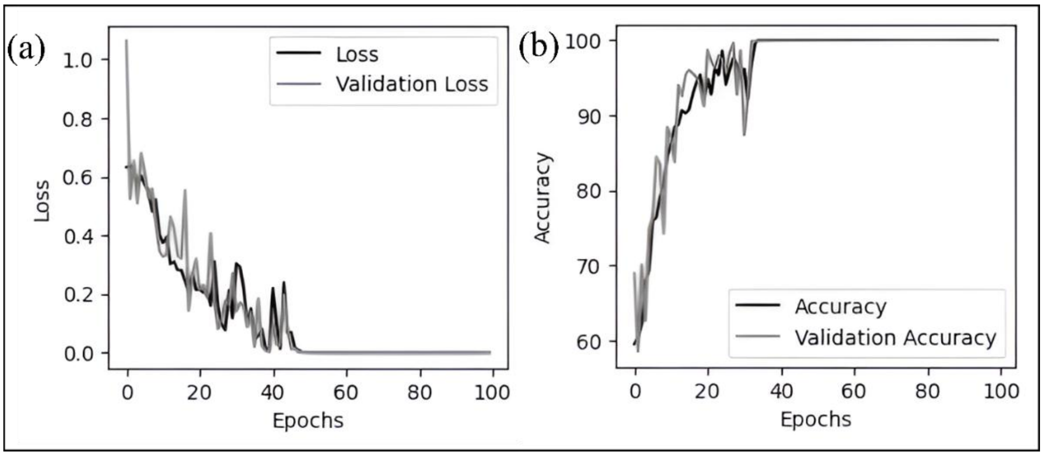

Fig. 14. Graphs of (a) Loss and (b)Accuracy of Augmented Images Classification during Training with The Xception Architecture

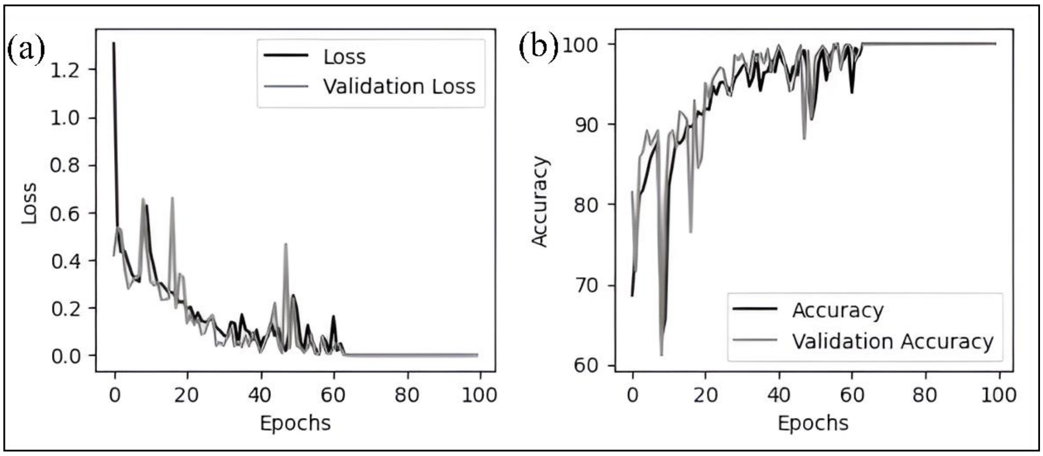

Fig. 15. Graphs of (a) Loss and (b)Accuracy of Augmented Images Classification during Training with The EfficientNet Architecture

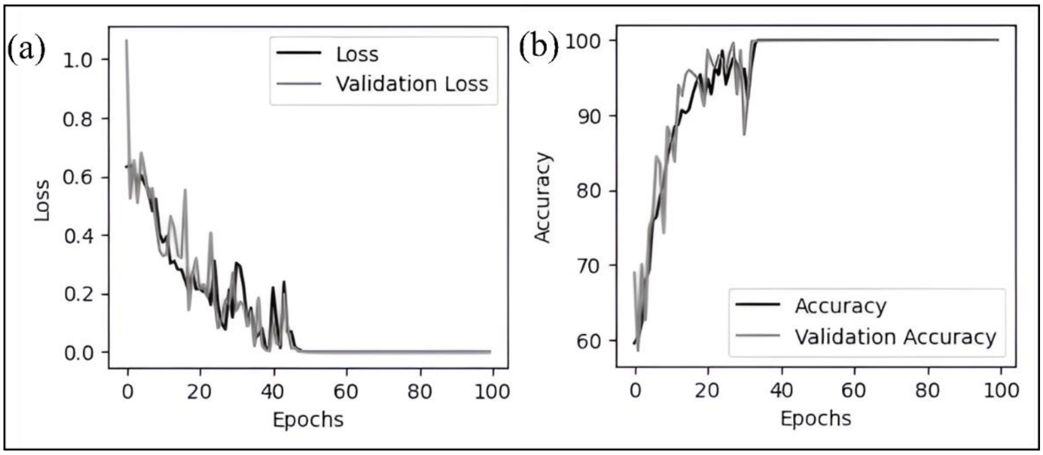

Fig. 16. Graphs of (a) Loss and (b)Accuracy of Augmented Images Classification during Training with The ResNet-50 Architecture

Color-enhanced Images

In this section, classification is performed using resized and color-enhanced images from the pre-processing stage. Classification includes training and testing. The color-enhanced images include 935 images of 425 viable flaps and 510 compromised flaps. Before the training process, the data was divided into 75% training data, comprising 701 images, and 25% testing data, comprising 234 images. The training data was further separated into 80% training data, comprising 560 images, and 20% validation data, comprising 141 images. Classification is carried out into two labels, viable and compromised flaps. Classification is carried out using several CNN architectures: DenseNet-201, Xception, EfficientNet, and ResNet-50 architectures. The parameters used in the training process with color-enhanced images are 100 epochs, a batch size of 5, and the Adam optimizer. During training, the accuracy of both the training and validation data is measured to evaluate the performance of the proposed classification models. Additionally, the loss value is assessed to quantify the error rate between predicted and actual labels. Accuracy and loss graphs from the original image classification training process using DenseNet-201, Xception, EfficientNet, and ResNet-50 architectures are presented in Figs. 17, 18, 19, and 20.

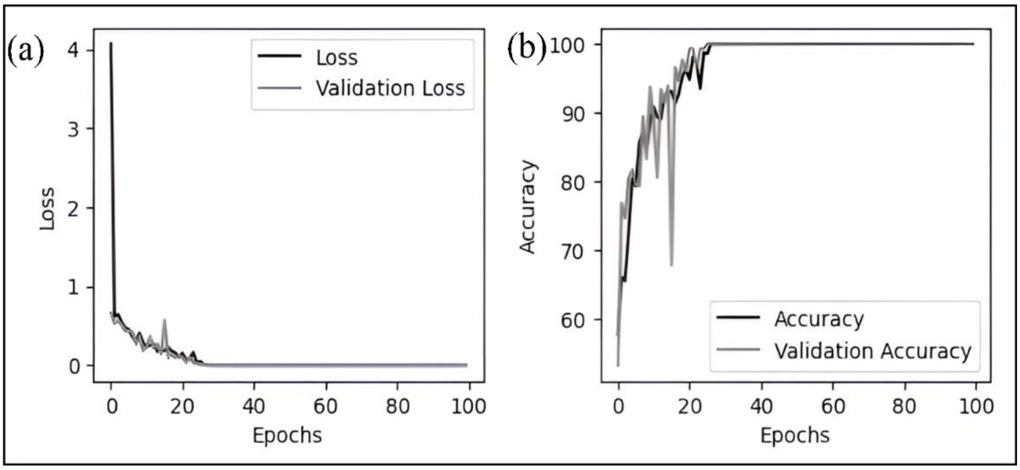

Fig. 17. Graphs of (a) Loss and (b)Accuracy of Enhanced Images Classification during Training with The DenseNet-201 Architecture

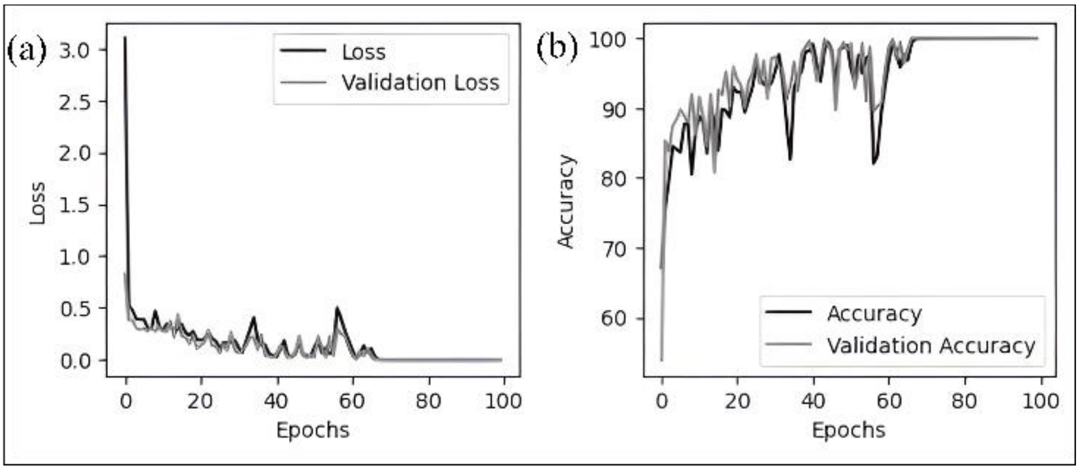

Fig. 18. Graphs of (a) Loss and (b)Accuracy of Enhanced Images Classification during Training with The Xception Architecture

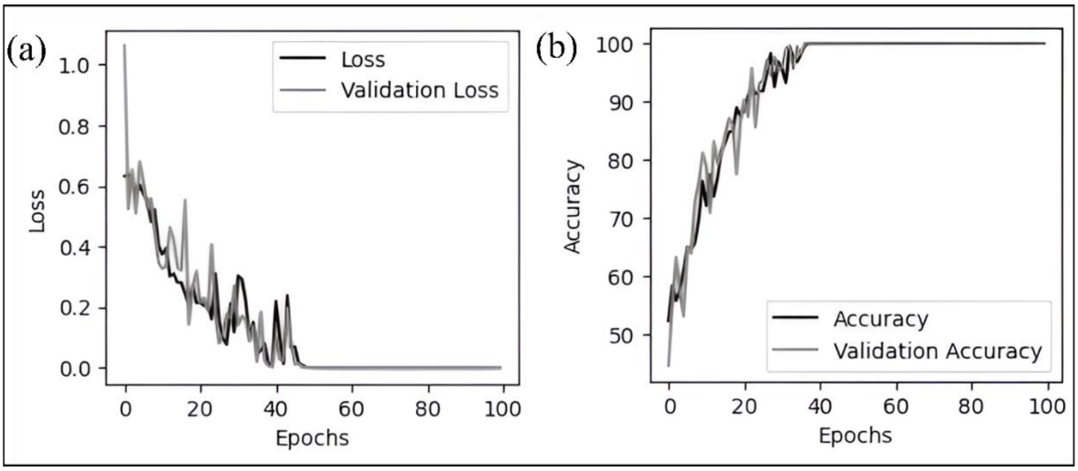

Fig. 19. Graphs of (a) Loss and (b)Accuracy of Enhanced Images Classification during Training with The EfficientNet Architecture

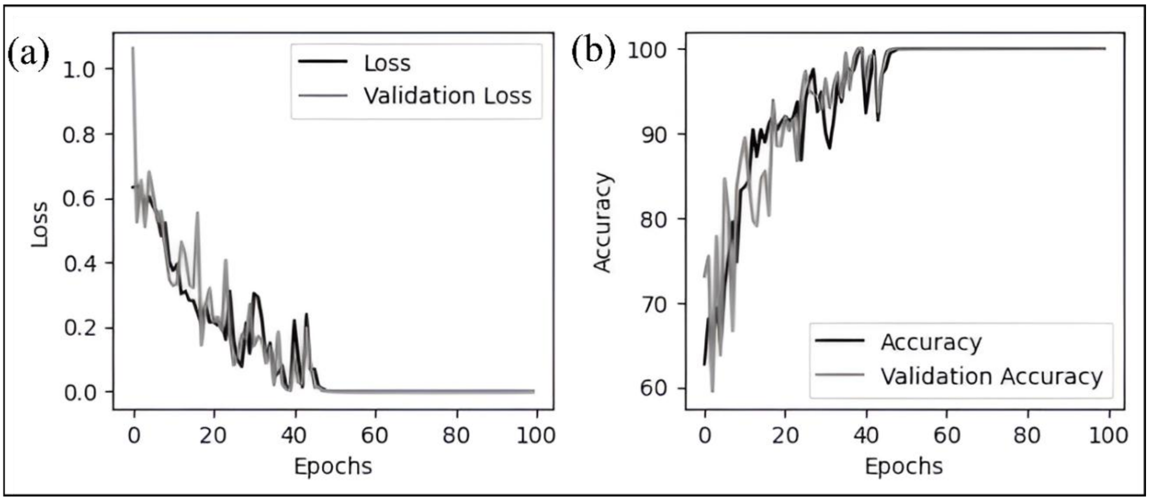

Fig. 20. Graphs of (a) Loss and (b)Accuracy of Enhanced Images Classification during Training with The ResNet-50 Architecture

Based on Figs. 17–20, the color-enhanced image classification training process using the DenseNet-201, Xception, EfficientNet, and ResNet-50 architectures shows fluctuating accuracy in both the training and validation datasets. In Fig. 17(b), 18(b), 19(b), and 20(b), the accuracy values of the DenseNet-201, Xception, EfficientNet, and ResNet-50 architectures stabilize at the 25th, 65th, 35th, and 45th epochs, respectively, reaching values above 95%. Based on Fig. 17(a), the training process of color-enhanced images classification using the DenseNet-201 architecture has a loss value that continues to decrease close to 0. Based on Fig. 18(a), 19(a), and 20(a), the training process of color-enhanced images classification using the Xception, EfficientNet, and ResNet-50 architectures shows a loss value that fluctuates and stabilizes at 65th and 45th epochs close to 0. The accuracy and loss values obtained during the training process show that these CNN architectures are capable of performing classification and have a low error rate.

C. Discussion and Analysis

In this study, a classification of viable and compromised flap images was carried out, consisting of training and testing stages. During training, classification using original, augmented, and color-enhanced images for each architecture achieved an accuracy above 98%. The loss value obtained is also close to 0. In the testing process, performance evaluations such as accuracy (Acc), sensitivity (Sen), specificity (Spe), and F1-score (F1) values for each group of images on each CNN architecture are measured. The overall performance evaluation results obtained in this study can be seen in Table 2.

Based on Table 2, it can be seen that the results of the classification of viable and compromised flap images have performance evaluation results such as good accuracy, sensitivity, specificity, and F1-score, namely above 98%. The accuracy value shows the proportion of labels that are predicted correctly. The sensitivity indicates the degree to which the proportion of viable flap labels is correctly predicted as viable flap labels by the model. Specificity indicates the degree to which the proportion of compromised flap labels is correctly predicted as compromised flap labels by the model. The F1-score shows the model's ability to perform classification by considering the balance between predicting all labels and minimizing prediction errors. This shows that the CNN architecture is able to classify viable and compromised flap images precisely and accurately. G-mean and MCC were also measured. The performance evaluation results for G-Mean and MCC are presented in Table 3.

TABLE II
PERFORMANCE EVALUATION ON VIABLE AND COMPROMISED FLAP IMAGES CLASSIFICATION WITH CNN ARCHITECTURES

No	Image	CNN Architecture	Performance Evaluation (%)			
			Acc	Sen	Spe	F1
1	Original Images	DenseNet-201	99	99	99	99
		Xception	99	98	98	99
		EfficientNet	99	99	99	99
		ResNet-50	99	99	99	99
2	Augmented Images	DenseNet-201	99	99	99	99
		Xception	99	99	99	99
		EfficientNet	99	99	99	99
		ResNet-50	99	99	99	99
3	Color-enhanced Images	DenseNet-201	99	99	99	99
		Xception	99	99	99	99
		EfficientNet	99	99	99	99
		ResNet-50	99	99	99	99

TABLE III
G-MEAN AND MCC EVALUATION ON VIABLE AND COMPROMISED FLAP IMAGES CLASSIFICATION WITH CNN ARCHITECTURES

No	Image	CNN Architecture	Performance Evaluation (%)	
			G-mean	MCC
1	Original Images	DenseNet-201	99	94.5
		Xception	98	93.5
		EfficientNet	99	95
		ResNet-50	99	93.6
2	Augmented Images	DenseNet-201	99	97.5
		Xception	99	96.3
		EfficientNet	99	94
		ResNet-50	99	97.5
3	Color-enhanced Images	DenseNet-201	99	94
		Xception	99	94
		EfficientNet	99	96
		ResNet-50	99	96

Based on Table 3, the evaluation results indicate that the classification performance for viable and compromised flap images demonstrates excellent G-mean results, consistently exceeding 97%. This finding underscores the efficacy of the CNN model in accurately classifying both viable and compromised flaps. Furthermore, the MCC evaluation reveals similarly strong performance, with values surpassing

93%, highlighting the model's ability to differentiate between the two label categories in a balanced and reliable manner. Collectively, these results confirm that the CNN model exhibits robust and accurate performance in classifying viable and compromised flap images.

IV. Conclusion

The pre-processing method used in this study includes resizing, augmentation, and color enhancement. The classification of viable and compromised flap images using several CNN architectures was carried out for each of the pre-processed images, namely original resized images, augmented images, and color-enhanced images. The classification of flap images was carried out using two labels, namely viable and compromised flaps. The CNN architectures used in the study include DenseNet-201, Xception, EfficientNet, and ResNet-50. The average performance evaluation results obtained by the CNN architectures in classifying each group of images resulting from pre-processing have a value above 98%. However, based on the accuracy and loss graphs obtained by each CNN architecture in the training process, it can be seen that the training process experienced overfitting in several epochs. The results of this study can be used to improve or further develop the CNN model in classifying viable and compromised flap images to provide better results and avoid overfitting. Good and precise flap image classification results can assist medical personnel in obtaining a more accurate diagnosis early when observing flap vitalility.

References

[1] A. M. Oyervides *et al.*, "Design and Testing of An Optical Instrument for Skin Flap Monitoring," *Sci. Rep.*, vol. 13, no. 1, pp. 1–10, 2023.

[2] E. Benanti, G. De Santis, A. L. Acciaro, G. Colzani, A. Baccarani, and M. Starnoni, "Soft Tissue Coverage of The Upper Limb: A Flap Reconstruction Overview," *Ann. Med. Surg.*, vol. 60, no. November, pp. 338–343, 2020.

[3] K. Odake, M. Tsujii, T. Iino, K. Chiba, T. Kataoka, and A. Sudo, "Febuxostat Treatment Attenuates Oxidative Stress and Inflammation due to Ischemia-Reperfusion Injury Through The Necrotic Pathway in Skin Flap of Animal Model," *Free Radic. Biol. Med.*, vol. 177, no. October, pp. 238–246, 2021.

[4] J. Yu *et al.*, "Unraveling The Potential of Nanozymes in The Tapestry of Orthopedic Healing," *Mater. Des.*, vol. 242, no. 113016, pp. 1–21, 2024.

[5] F. J. Paprottka, A. E. J. Trevatt, D. Klimas, N. Krezdorn, and D. Schlarb, "Cook - Swartz Doppler Probe Surveillance for Free Flaps - De fining Pros and Cons," *Surg. J.*, vol. 1, no. 212, pp. 42–46, 2020.

[6] A. Mishra *et al.*, "Oncologic Safety of Submental Island Flap Reconstruction in Clinically Node-Negative Oral Cancer Patients: A Prospective Comparative Study," *Int. J. Oral Maxillofac. Surg.*, vol. 51, no. 2, pp. 159–165, 2022.

[7] J. H. Park and J. U. Park, "Flap Monitoring with Incisional Negative Pressure Wound Therapy (NPWT) in Diabetic Foot Patients," *Sci. Rep.*, vol. 12, no. 1, pp. 1–8, 2022.

[8] D. P. Mishra, S. Mishra, S. Jena, and S. R. Salkuti, "Image Classification using Machine Learning," *Indones. J. Electr. Eng. Comput. Sci.*, vol. 31, no. 3, pp. 1551–1558, 2023.

[9] P. H. Putra, M. S. Novelan, and M. Rizki, "Analysis K-Nearest Neighbor Method in Classification of Vegetable Quality Based on Color," *J. Appl. Eng. Technol. Sci.*, vol. 3, no. 2, pp. 126–132, 2022.

[10] A. Desiani *et al.*, "Multi-Stage CNN: U-Net and Xcep-Dense of Glaucoma Detection in Retinal Images," *J. Electron. Electromed. Eng. Med. Informatics*, vol. 5, no. 4, pp. 211–222, 2023.

[11] D. Ahmedt-Aristizabal *et al.*, "Deep learning Approaches for Seizure Video Analysis: A Review," *Epilepsy Behav.*, vol. 154, no. 109735, pp. 1–21, 2024, doi: 10.1016/j.yebeh.2024.109735.

[12] Lifeng Zhang, and Ying Tian, "Research on Vehicle Detection Algorithms Based on YOLOv5s," *IAENG International Journal of Computer Science*, vol. 50, no.4, pp1453–1459, 2023.

[13] L. Atika, S. Nurmaini, R. U. Partan, and E. Sukandi, "Image Segmentation for Mitral Regurgitation with Convolutional Neural Network Based on UNet, Resnet, Vnet, FractalNet and SegNet: A Preliminary Study," *Big Data Cogn. Comput.*, vol. 6, no. 4, pp. 1–20, 2022.

[14] G. Zeng *et al.*, "Deep Convolutional Neural Networks for Aged Microplastics Identification by Fourier Transform Infrared Spectra Classification," *Sci. Total Environ.*, vol. 913, no. 169623, pp. 1–13, 2024.

[15] D. K. Jain, K. Gupta, V. Bajaj, and A. Hussain, "Multi-Model Deep Learning System for Screening Human Monkeypox Using Skin Images," *Expert Syst.*, pp. 1–16, 2024.

[16] S. Gujarathi, R. Shrivastava, and S. K. Angadi, "A Survey of Kidney Cancer Analysis Using Machine Learning and Deep Learning Algorithms," *J. Electr. Syst.*, vol. 20, no. 6, pp. 2491–2501, 2024.

[17] O. Saidani *et al.*, "White Blood Cells Classification Using Multi-Fold Pre-Processing and Optimized CNN Model," *Sci. Rep.*, vol. 14, no. 3570, pp. 1–14, 2024.

[18] D. A. Arafa, H. E. D. Moustafa, H. A. Ali, A. M. T. Ali-Eldin, and S. F. Saraya, *A Deep Learning Framework for Early Diagnosis of Alzheimer's Disease on MRI Images*, vol. 83, no. 2. Springer US, 2024.

[19] S. H. Khaleefah *et al.*, "Applying Deep Learning Models to Breast Ultrasound Images for Automating Breast Cancer Diagnosis," *Int. J. Informatics Vis.*, vol. 8, no. 3–2, pp. 1779–1783, 2024, doi: 10.62527/joiv.8.3-2.1912.

[20] M. M. Musthafa, M. T R, V. K. V, and S. Guluwadi, "Enhanced Skin Cancer Diagnosis Using Optimized CNN Architecture and Checkpoints for Automated Dermatological Lesion Classification," *BMC Med. Imaging*, vol. 24, no. 201, pp. 1–20, 2024.

[21] H. A. Salman and A. Kalakech, "Image Enhancement using Convolution Neural Networks," *Babylonian J. Mach. Learn.*, vol. 2024, pp. 30–47, 2024.

[22] R. Shanmukh, N. Raju, N. K. Challa, and M. Mukesh, "A Comparative Analysis of CNN Techniques on Application to Fundus Images," *J. Chem. Heal. Risks*, vol. 13, no. 6, pp. 2086–2090, 2023.

[23] I. U. Khan and J. W. Lee, "PAR-Net: An Enhanced Dual-Stream CNN–ESN Architecture for Human Physical Activity Recognition," *Sensors*, vol. 24, no. 6, pp. 1–21, 2024.

[24] H. Halit and İ. Ibrahim, "Classification of Cataract Disease with a DenseNet201 Based Deep Learning Model," *J. Inst. Sci. Technol.*, vol. 12, no. 3, pp. 1264–1276, 2022.

[25] L. Moataz, G. I. Salama, and M. H. A. Elazeem, "Skin Cancer Diseases Classification using Deep Convolutional Neural Network with Transfer Learning Model," *J. Phys. Conf. Ser.*, vol. 2128, no. 1, pp. 1–11, 2021.

[26] F. Zulfiqar, U. I. Bajwa, and Y. Mehmood, "Multi-Class Classification of Brain Tumor Types from MR Images using EfficientNets," *Biomed. Signal Process. Control*, vol. 84, no. February, p. 104777, 2023.

[27] L. I. Kesuma and R. Rudiansyah, "Classification of Covid-19 Diseases Through Lung CT-Scan Image Using the ResNet-50 Architecture," *Comput. Eng. Appl. J.*, vol. 12, no. 1, pp. 11–30, 2023.

[28] L. Widyawati, I. Riadi, and Y. Prayudi, "Comparative Analysis of Image Steganography using SLT, DCT and SLT-DCT Algorithm," *MATRIK J. Manajemen, Tek. Inform. dan Rekayasa Komput.*, vol. 20, no. 1, pp. 169–182, 2020.

[29] D. S. Y. Kartika, A. Wulansari, H. Maulana, A. M. Rizki, and A. L. Nurlaili, "Digital Image Segmentation Resulting from X-Rays of Covid Patients using K-Means and Extraction Features Method," *Ijconsist Journals*, vol. 3, no. 1, pp. 25–28, 2021.

[30] M. Arhami, Y. R. Fachri, H. Hendrawaty, and A. Adriana, "A Semantic Segmentation of Nucleus and Cytoplasm in Pap-smear Images using Modified U-Net Architecture," *Infotel*, vol. 16, no. 2, pp. 273–288, 2024.

[31] S. I. Maiyanti *et al.*, "Rotation-Gamma Correction Augmentation on CNN-Dense Block for Soil Image Classification," *Appl. Comput. Sci.*, vol. 19, no. 3, pp. 96–115, 2023.

[32] I. Kurniastuti, E. N. I. Yuliati, F. Yudianto, and T. D. Wulan, "Determination of Hue Saturation Value (HSV) Color Feature in Kidney Histology Image," *J. Phys. Conf. Ser.*, vol. 2157, no. 1, pp. 1–9, 2022.

[33] C. Bhardwaj, S. Jain, and M. Sood, "Diabetic Retinopathy Severity Grading Employing Quadrant-Based Inception-V3 Convolution Neural Network Architecture," *Int. J. Imaging Syst. Technol.*, vol. 31, no. 2, pp. 592–608, 2021.

[34] Haoyan Jiang, and Ji Zhao, "Multi-lesion Segmentation of Fundus Images using," *IAENG International Journal of Computer Science*,

vol. 51, no.10, pp1587–1595, 2024.
[35] Kang Tan, Linna Li, and Qiongdan Huang, “Image Manipulation Detection Using the Attention Mechanism and Faster R-CNN,” *IAENG International Journal of Computer Science*, vol. 50, no.4, pp1261–1268, 2023.
[36] M. D. Bloice, P. M. Roth, and A. Holzinger, “Biomedical Image Augmentation using Augmentor,” *Bioinformatics*, vol. 35, no. 21, pp. 4522–4524, 2019.
[37] F. Garcea, A. Serra, F. Lamberti, and L. Morra, “Data Augmentation for Medical Imaging: A Systematic Literature Review,” *Comput. Biol. Med.*, vol. 152, no. December 2022, p. 106391, 2023.
[38] D. Lee, H. Park, T. Pham, and C. D. Yoo, “Learning Augmentation Network via Influence Functions,” in *Proceedings of the IEEE Computer Society Conference on Computer Vision and Pattern Recognition*, 2020, pp. 10958–10967.
[39] Jiali Sun, Shaochuan Xu, Dehua Liu, and Jing He, “Design of Belt No-load Detection System Based on Image Processing Technology,” *IAENG International Journal of Computer Science*, vol. 51, no.11, pp1731–1739, 2024.
[40] M. H. M. Teodorescu, L. Morse, Y. Awwad, and G. C. Kane, “Failures of Fairness in Automation Require A Deeper Understanding of Human–ML Augmentation,” *MIS Q. Manag. Inf. Syst.*, vol. 45, no. 3, pp. 1483–1499, 2021.
[41] D. Zhao, L. Zhao, R. Ma, and X. Zhao, “Research on Traffic Sign Detection Algorithm Based on Improved YOLOv3,” *J. Phys. Conf. Ser.*, vol. 2026, no. 1, pp. 1–9, 2021.
[42] A. K. Nugroho, R. Wardoyo, M. E. Wibowo, and H. Soebono, “Image Dermoscopy Skin Lesion Classification using Deep Learning Method: Systematic Literature Review,” *Bull. Electr. Eng. Informatics*, vol. 13, no. 2, pp. 1042–1049, 2024.
[43] Haitian Qin, Yang Xu, and Xupeng Chen, “A Multi-Resolution Feature Fusion Method for Pedestrian Re-identification,” *IAENG International Journal of Computer Science*, vol. 51, no.9, pp1393–1403, 2024.
[44] Y. Kateb, H. Meglouli, and A. Khebli, “Coronavirus Diagnosis Based on Chest X-Ray Images and Pre-Trained DenseNet-121,” *Rev. d’Intelligence Artif.*, vol. 37, no. 1, pp. 23–28, 2023.
[45] Hang Sun, and Ziwei Zhou, “Structured Light Center Extraction Study with Multiple Attention Mechanisms,” *IAENG International Journal of Computer Science*, vol. 51, no.4, pp437–446, 2024.
[46] Xiaoqing Sun, Wenhua Cui, Ye Tao, and Zhaoyang Wang, “Flame Image Detection Algorithm Based on Computer Vision,” *IAENG International Journal of Computer Science*, vol. 50, no.4, pp1142–1158, 2023.
[47] Marina Popolizao, Alberto Amato, Federico Liquori, Tiziano Politi, Alessandro Quarto, And Vincenzo Di Lecce, “The GAIN Method for the Completion of Multidimensional Numerical Series of Meteorological Data,” *IAENG International Journal of Computer Science*, vol. 48, no.3, pp496–506, 2021.
[48] Ren Guo-Xi, “Research on a Convolutional Neural Network Method for Modulation Waveform Classification,” *IAENG International Journal of Computer Science*, vol. 50, no.3, pp875–882, 2023.
[49] Anita Desiani, Erwin, Bambang Suprihatin, Sugandi Yahdin, Ajeng I. Putri, and Fathur R. Husein, “Bi-Path Architecture of CNN Segmentation and Classification Method for Cervical Cancer Disorders Based on Pap-smear Images,” *IAENG International Journal of Computer Science*, vol. 48, no.3, pp782–791, 2021.
[50] S. Ioffe and C. Szegedy, “Batch Normalization: Accelerating Deep Network Training by Reducing Internal Covariate Shift,” *Journal. Pract.*, vol. 10, no. 6, pp. 730–743, 2016.
[51] L. Li, Z. Yang, X. Yang, J. Li, and Q. Zhou, “PV Resource Evaluation Based on Xception and VGG19 Two-Layer Network Algorithm,” *Heliyon*, vol. 9, no. 11, pp. 1–12, 2023.
[52] Yuanbin Wang, Bingchao Wu, and Zongyou Duan, “Insulator Self-Explosion Detection Based on Mixed Samples and Transfer Learning,” *IAENG International Journal of Computer Science*, vol. 51, no.10, pp1579–1586, 2024.
[53] H. Chen, Y. Yang, and S. Zhang, “Learning Robust Scene Classification Model with Data Augmentation Based on Xception,” *J. Phys. Conf. Ser.*, vol. 1575, no. 1, pp. 1–7, 2020.
[54] L. Alzubaidi *et al.*, *Review of Deep Learning: Concepts, CNN Architectures, Challenges, Applications, Future Directions*, vol. 8, no. 53. Springer International Publishing, 2021.
[55] E. Paladini, E. Vantaggiato, F. Bougourzi, C. Distante, A. Hadid, and A. Taleb-Ahmed, “Two Ensemble-CNN Approaches for Colorectal Cancer Tissue Type Classification,” *J. Imaging*, vol. 7, no. 51, pp. 1–21, 2021.
[56] T. A. Soomro *et al.*, “Deep Learning Models for Retinal Blood Vessels Segmentation: A Review,” *IEEE Access*, vol. 7, pp. 71696–71717, 2019.
[57] Xinling Feng, Cuiqing Zhu, and Zixia Ge, “Research on Low Resolution Digital Image Reconstruction Method Based on Rational Function Model,” *IAENG International Journal of Computer Science*, vol. 51, no.2, pp75–82, 2024.
[58] I. Markoulidakis, G. Kopsiaftis, I. Rallis, and I. Georgoulas, “Multi-Class Confusion Matrix Reduction Method and Its Application on Net Promoter Score classification problem,” in *ACM International Conference Proceeding Series*, 2021, pp. 412–419.
[59] J. H. J. C. Ortega, A. C. Lagman, L. R. Q. Natividad, E. T. Bantug, M. R. Resureccion, and L. O. Manalo, “Analysis of Performance of Classification Algorithms in Mushroom Poisonous Detection using Confusion Matrix Analysis,” *Int. J. Adv. Trends Comput. Sci. Eng.*, vol. 9, no. 1.3, pp. 451–456, 2020.
[60] N. Maleki, Y. Zeinali, and S. T. A. Niaki, “A K-NN Method for Lung Cancer Prognosis with The Use of A Genetic Algorithm for Feature Selection,” *Expert Syst. Appl.*, vol. 164, no. July 2019, p. 113981, 2021.
[61] J. Huang *et al.*, “DBFU-Net: Double Branch Fusion U- Net with Hard Example Weighting Train Strategy to Segment Retinal Vessel,” *PeerJ Comput. Sci.*, vol. 8, pp. 1–29, 2022.
[62] A. S. Desuky, S. Hussain, and M. A. Cifci, “Parameter Optimization Based Mud Ring Algorithm for Improving the Maternal Health Risk Prediction,” *IEEE Access*, vol. 12, pp. 167245–167261, 2024.
[63] G. Dheepak, J. A. Christaline, and D. Vaishali, “MEHW-SVM Multi-Kernel Approach for Improved Brain Tumour Classification,” *IET Image Process.*, vol. 18, pp. 856–874, 2024,
[64] F. Rahmad, Y. Suryanto, and K. Ramli, “Performance Comparison of Anti-Spam Technology Using Confusion Matrix Classification,” in *IOP Conference Series: Materials Science and Engineering*, 2020, vol. 879, no. 1.

Dite Geovani was born in Palembang, Januari 2002. She is currently working on a project for Doctoral Program at Engineering Faculty, Universitas Sriwijaya. She received a bachelor's degree in Mathematics from Universitas Sriwijaya in 2023 and has currently undergoing a PMDSU scholarship program at Universitas Sriwijaya since 2023. Her current research includes the fields of image processing, pattern recognition, data mining, and artificial intelligence.

Siti Nurmaini was born in Palembang, Indonesia, in 1969. This author became a Member (M) of IAENG in 2011. She received a bachelor’s degree in Electrical Engineering from Universitas Sriwijaya in 1992, and master's degree in Control System from Institut Teknologi Bandung, Indonesia, in 1998, and a Ph.D. degree in Computer Science from Universiti Teknologi Malaysia in 2011. In 1995. She joined the Department of Informatics, Faculty of Computer Science, Universitas Sriwijaya as an Associate Professor. Her current research interests include; deep learning, machine learning, robotics, and medical.

Anita Desiani was born in Palembang, Indonesia, in 1977. She received a bachelor’s degree in Mathematics from Universitas Sriwijaya in 2000, and master's degree in Computer Science from Universitas Gadjah Mada in 2003, and a Ph.D. degree in Mathematics and Natural Science Faculty, from Universitas Sriwijaya in 2023. In the same year, she joined as a lecturer at the Mathematics Department at Universitas Sriwijaya until now. Her current research interests include the fields of data mining, image processing, pattern recognition, computer vision, and artificial intelligence.

Mufida Muzakkie is currently working on a project for the Doctoral Program at the Medical Faculty, Universitas Sriwijaya. She received her bachelor's degree in medicine from Universitas Yarsi in 2008 and her medical profession from Universitas Yarsi in 2010. Her current research includes the field of medical imaging and surgery.